Chapter-5

Highly Porous, Anhydrous $Co_{0.5}Ni_{0.5}C_2O_4$ for Pseudocapacitive Energy Storage Applications

5.1 Introduction

Many studies are being carried out on transition metal oxide-based materials such as NiO, V_2O_5, spinel Co_3O_4, Fe_2O_3, and mixed spinel $NiCo_2O_4$ to explore electrodes for the pseudocapacitor.[1-7] However, structural instability and performance degradation issues related to transition metal oxide lead to the investigation of a novel framework structure for higher surface charge storage and better structural stability.[8-10] Metal–organic frameworks (MOFs) are used as an interesting open framework structure, where materials are constructed by joining metal-containing units with organic linkers, generating an interesting three-dimensional or two-dimensional network with permanent porosity.[11] Highly porous metal–organic framework structures, especially utilizing an oxalate linker with active participation metal ion redox, are known to show faradic pseudocapacitive characteristics.[12-14] However, most oxalate materials have a high open structural space to accommodate the hydration of water. We have envisaged the controlled removal of structural water from the material to develop a novel porous structure that can accommodate a high degree of charge or anion intercalation/deintercalation couple with double layer capacitance to achieve superior capacitance.[9b] The controlled water removal can maintain the high porosity of the structure that can enable fast charge/ion transfer.

Here, in this chapter, we present the synthesis, characterizations, and electrochemical performances of hydrated $Co_{0.5}Ni_{0.5}C_2O4{\cdot}2H_2O$ and porous anhydrous $Co_{0.5}Ni_{0.5}C_2O_4$ electrodes. The porous anhydrous $Co_{0.5}Ni_{0.5}C_2O_4$ electrode shows the specific capacitance value of 2396 F/g at 1 A/g, whereas hydrated $Co_{0.5}Ni_{0.5}C_2O4{\cdot}2H_2O$ shows the capacitance equivalent to 810 F/g at 1 A/g in an aqueous 2 M KOH electrolyte. Furthermore, we assembled aqueous asymmetric supercapacitors (ASCs), in which porous anhydrous $Co_{0.5}Ni_{0.5}C_2O_4$ was used as the positive electrode and activated carbon (AC) was utilized as the negative electrode. The highest specific energy equivalent to 283 W h/kg and specific

power of ~817 W/kg were achieved at 1 A/g current rates by the combination of porous anhydrous $Co_{0.5}Ni_{0.5}C_2O_4$ and AC with high cyclic stability.

5.2 Material synthesis and characterization

5.2.1 Synthesis

Synthesis of $Co_{0.5}Ni_{0.5}C_2O4{\cdot}2H_2O$ was carried out by the precipitation method. Highly porous anhydrous $Co_{0.5}Ni_{0.5}C_2O_4$ was prepared in a two-step synthesis. 1.49 g of cobalt(II) nitrate hexahydrate ($Co(NO_3)_2{\cdot}6H_2O$) and 1.46 g of nickel(II) nitrate hexahydrate ($Ni(NO_3)_2{\cdot}6H_2O$) were dissolved in 200 mL of deionized water with continuous stirring using a hot plate magnetic stirrer, and 1.27 g of oxalic acid dehydrate ($H_2C_2O_4{\cdot}2H_2O$) was added in solution. The entire mixture was stirred vigorously at 80 °C for 5 h. After 5 h of stirring, a white color precipitate of product $Co_{0.5}Ni_{0.5}C_2O4{\cdot}2H_2O$ was obtained. The obtained product is then washed several times with deionized water. Finally, the washed product, $Co_{0.5}Ni_{0.5}C_2O4{\cdot}2H_2O$, was dried in a hot air oven at 90 °C overnight. Porous anhydrous $Co_{0.5}Ni_{0.5}C_2O_4$ was formed after heating the material at 230 °C for 5 h in an N_2 atmosphere.

$$0.5Co(NO_3)_2.6H_2O + 0.5Ni(NO_3)_2.6H_2O + H_2C_2O_4.2H_2O \longrightarrow Co_{0.5}Ni_{0.5}C_2O_4.2H_2O \downarrow + 2HNO_3 + 2H_2O \quad \text{at } 80^oC \qquad (5.1).$$

$$Co_{0.5}Ni_{0.5}C_2O_4.2H_2O \longrightarrow Co_{0.5}Ni_{0.5}CO_4 + 2H_2O \uparrow \quad \text{at } 210^oC \qquad (5.2)$$

5.2.2 Characterizations

The crystal structure and phase purity of synthesized products were characterized through a Rigaku Miniflex desktop X-ray diffractometer (XRD) with Cu-Ka radiation (λ = 0.154 nm) in the range of 2θ = 10−90° with a step size of 0.02°. Xpert High Score (PANanylytical) software was used to identify the required phase. FE-SEM (FP 5022/22) was used to determine the surface morphology and structure of the sample. Infrared spectra of the samples were recorded using a Nicolet iS5 FTIR spectrometer in the range of 400−4000 cm−1. Pore size distribution and specific surface area of the sample were measured by BET

(MicrotracBEL). All electrochemical performances of the sample including cyclic voltammetry (CV), galvanostatic charge-discharge (GCD), and electrochemical impedance spectroscopy (EIS) were conducted using a conventional three-electrode arrangement measured by Metrohm Autolab (PGSTAT204) equipped with a FRA32M module. Electrochemical measurements were analyzed using NOVA1.1 software.

5.2.3 Preparation of Electrode:

Hydrated $Co_{0.5}Ni_{0.5}C_2O4{\cdot}2H_2O$ and anhydrous porous $Co_{0.5}Ni_{0.5}C_2O_4$ working electrodes were prepared in a 7:2:1 ratio of the active material, activated carbon, and binder (PVDF) in NMP solvent. The homogenous slurry was prepared using a mortar, and slurry containing ~1 mg of active materials was cast over a 1 cm^2 area of Toray carbon paper. The coated electrode was dried at 80°C for 12 h. The electrode loading was calculated by taking the weight of the electrode using an electronic balance (error limit: 0.01 mg). For that, the weight of Torrey paper was taken first, and then, the weight of the coated electrode (after drying the coated ink on Torrey carbon paper on a 1 × 1 cm^2 area) was taken for the study. Then, from the difference in the weight, the exact loading of the electrode material was calculated.

5.3 XRD Study

The XRD peak pattern of $Co_{0.5}Ni_{0.5}C_2O4{\cdot}2H_2O$ and anhydrous $Co_{0.5}Ni_{0.5}C_2O_4$ powder confirms the phase purity and formation of the single-phase material. Figure 1a shows the XRD plot of $Co_{0.5}Ni_{0.5}C_2O4{\cdot}2H_2O$ and anhydrous $Co_{0.5}Ni_{0.5}C_2O_4$ in the 2θ range of 10−60° with a step size of 0.02°. The prominent sharp diffraction peaks at 18.84, 22.78, 30.35, 35.6, and 49.08 represent the (202), (004), (400), (022), and (602) planes of $Co_{0.5}Ni_{0.5}C_2O4{\cdot}2H_2O$ in the orthorhombic cell (space group: Cccm) and matches very well with the diffraction pattern of $NiC_2O_4{\cdot}2H_2O$ (JCPDS no. 25- 0582).[15-16] After annealing at 230 °C for 5 h, $Co_{0.5}Ni_{0.5}C_2O4{\cdot}2H_2O$ transformed into anhydrous $Co_{0.5}Ni_{0.5}C_2O_4$ in the α-monoclinic

structure (space group P21/n, JCPDS no.: 37-0719). Figure 5.1(b) shows the Rietveld Refined XRD profile of $Co_{0.5}Ni_{0.5}C_2O_4$ with lattice parameters a = 5.234 Å, b = 5.653 Å, c = 7.159 Å, α-90°, β- 118.88°, and γ-90°, and the VESTA image is shown in the inset.[17] Crystal structure of anhydrous $Co_{0.5}Ni_{0.5}C_2O_4$ showing tunneles for interclation is presented in fig 5.1(c)

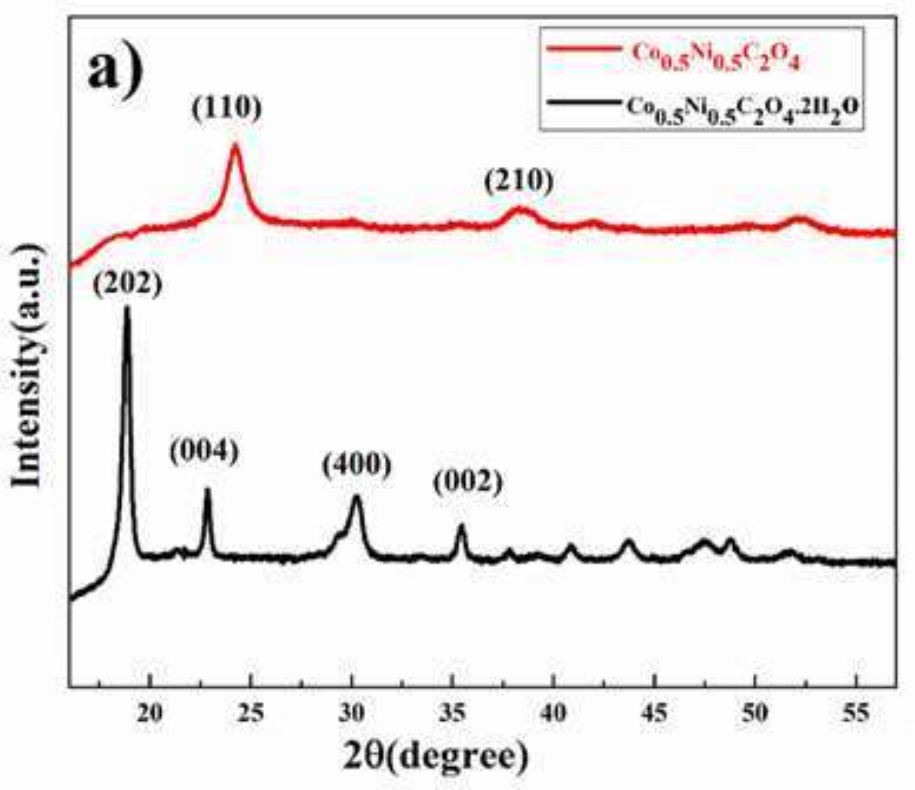

Figure 5.1: (a) XRD pattern of $Co_{0.5}Ni_{0.5}C_2O4{\cdot}2H_2O$ and $Co_{0.5}Ni_{0.5}C_2O_4$,

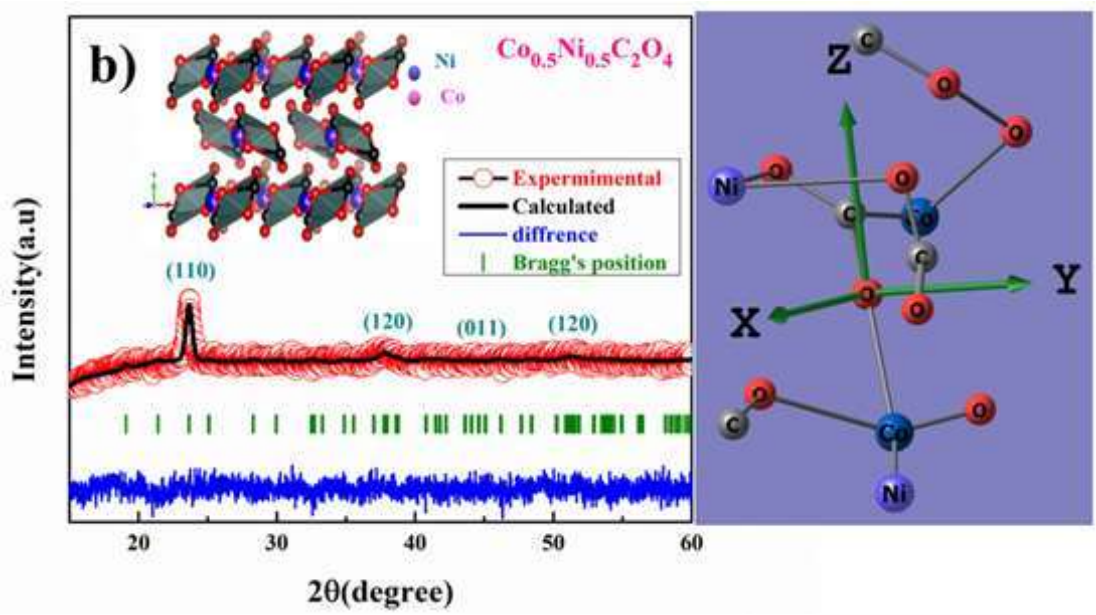

Figure 5.1: (b) Rietveld refinement of the XRD profile of anhydrous $Co_{0.5}Ni_{0.5}C_2O_4$ (vista image in the inset)

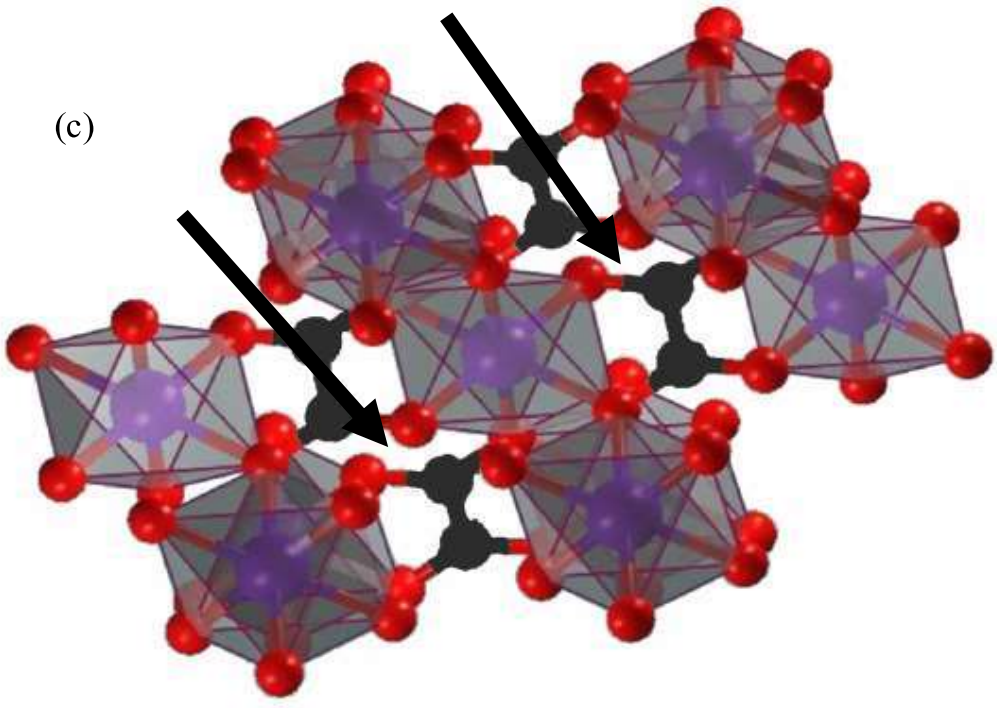

Figure 5.1:(c) Crystal structure of anhydrous $Co_{0.5}Ni_{0.5}C_2O_4$ showing tunneles for interclation

5.4 Thermal study

Thermogravimetric analysis (TGA) as shown in Figure 5.1(d) was used to understand the thermal stability of $Co_{0.5}Ni_{0.5}C_2O4{\cdot}2H_2O$. The first weight loss occurred at the temperature from 100 to 300 °C, which corresponds to the removal of structural water from the sample; in this temperature range, phase transformation also occurred from orthorhombic to monoclinic. The TGA curve determines the weight loss of 27%, as 2 mol of water was removed from the sample in the temperature range of 100−300 °C. DTA shown in the inset clearly shows structure water leaving the structure at 219 °C, and the second weight loss step or decomposition of the oxalate group occurs in the temperature range of 350−500 °C, in which the weight loss of 35% was observed for decomposition of $Co_{0.5}Ni_{0.5}C_2O_4$. That is why to perform the control dehydration of materials we carried out dehydration or annealing at 230 °C to avoid rapid loss of structure water that can damage the porous structure and can result in particle segregation. Thus, to protect the porous structure of the anhydrous material, annealing was carried out at 230 °C in an N_2 atmosphere.

Weight loss steps can be represented as follows

$$Co_{0.5}Ni_{0.5}CO_4.2H_2O \rightarrow Co_{0.5}Ni_{0.5}CO_4 + 2H_2O \quad (\text{above } T\sim200\ ^oC) \tag{5.3}$$

$$Co_{0.5}Ni_{0.5}CO_4 \rightarrow Co_{0.5}Ni_{0.5}O + 2CO_2 \quad (\text{above } T \geq 450\ ^oC) \tag{5.4}$$

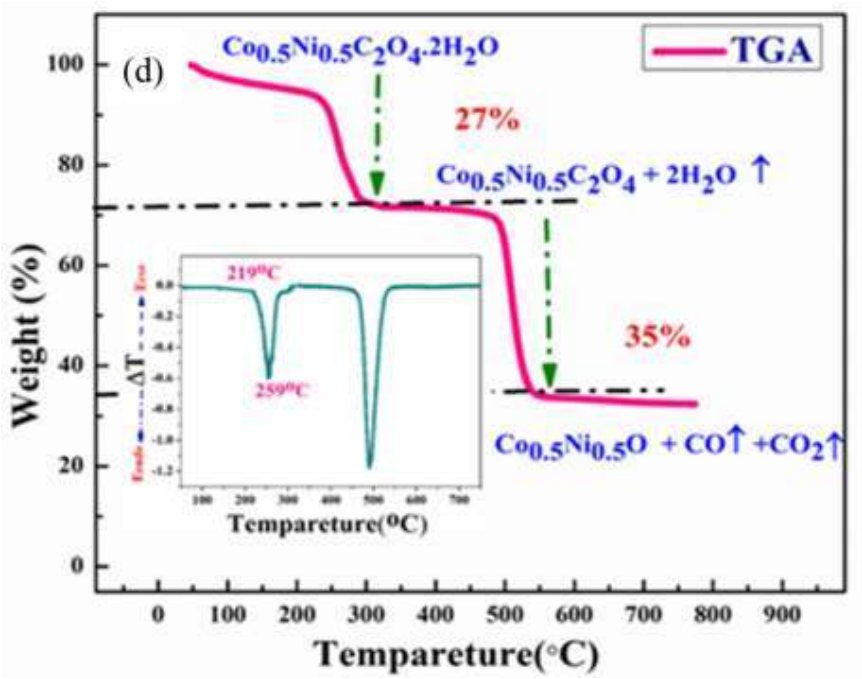

Figure 5.1: (d)TGA of $Co_{0.5}Ni_{0.5}C_2O4{\cdot}2H_2O$ in an N_2 atmosphere (inset shows the DTA plot),

FTIR spectra of $Co_{0.5}Ni_{0.5}C_2O4{\cdot}2H_2O$ and anhydrous $Co_{0.5}Ni_{0.5}C_2O_4$ powder samples shown in Figure 5.1(e) reveal the presence of different functional groups in the material. The broad peak at 3381.71 cm^{-1} belongs to the stretching vibration of the hydroxyl group (−OH), which signifies the presence of water in $Co_{0.5}Ni_{0.5}C_2O4{\cdot}2H_2O$. The observed peak at 1620.75 cm^{-1} was assigned to the antisymmetric carbonyl stretching band (C=O) specific to the oxalate group.[17] Two weak peaks at 1326.86 and 1310.75 cm^{-1} were attributed to vibrations of $C_2O_4^{2-}$ (C−O) + (C−C) and (C−O) + (O−C=O), respectively. The peak at 829.16 cm^{-1} was assigned to the vibration mode of $C2O4^{2-}$ and O−C=O bending vibrations (O−C=O). The absorption peak at 478.19 cm^{-1} can be attributed to both Ni–O and Co−O bonding present in the prepared sample of Cobalt oxalate dehydrate ($Co_{0.5}Ni_{0.5}C_2O_4{\cdot}2H_2O$). The annealing product after structural water removal represents $Co_{0.5}Ni_{0.5}C_2O_4$. The FT-IR study clearly shows the distinctive decrease in peak intensity of stretching vibration of the hydroxyl group (−OH) near 3381.73 cm^{-1}.[14]

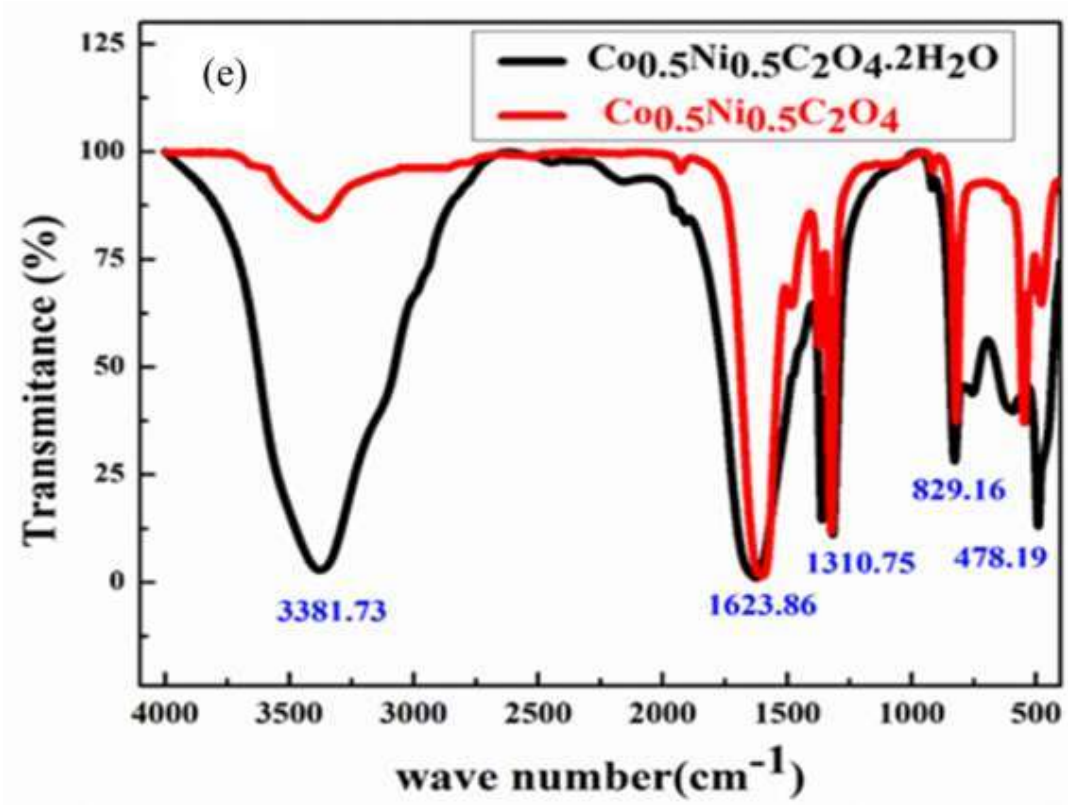

Figure.5.1: (e) FT-IR spectra of $Ni_{0.5}Co_{0.5}C_2O_4 \cdot 2H_2O$ and $Co_{0.5}Ni_{0.5}C_2O_4$,

The BET results of the $Co_{0.5}Ni_{0.5}C_2O_4$ sample shows in Figure 5.1(f). The nitrogen adsorption and desorption isotherm show characteristics, which correspond to the mesoporous structure of the oxalate; $Co_{0.5}Ni_{0.5}C_2O_4$ sample. The calculated BET-specific surface area and average pore diameter are 129.82 m^2/g and 1.5−3.92 nm, respectively with the appearance of both micropores and mesopores. Mesoporous structures attribute to excellent electrochemical kinetics due to high porosity. The calculated pore diameter of the $Co_{0.5}Ni_{0.5}C_2O_4$ sample is much higher than that of the ions present in aqueous electrolytes.[15-16]

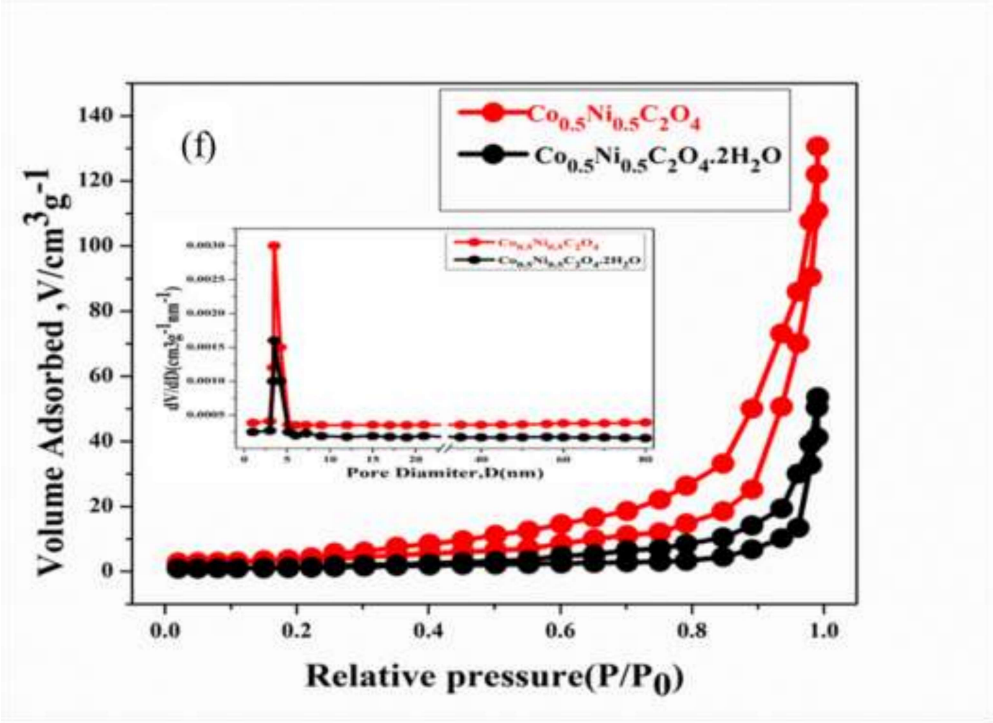

Figure.5.1:(f) BET surface area measurement plot of $Co_{0.5}Ni_{0.5}C_2O_4 \cdot 2H_2O$ and $Co_{0.5}Ni_{0.5}C_2O_4$.

Figure 5.2(a) shows the X-ray photoelectron spectroscopy (XPS) survey plot of the $Co_{0.5}Ni_{0.5}C_2O_4$ sample, further confirming the presence of Ni and Co in the material. The Ni (2p) spectrum shown in Figure 5.2(b) could be assigned to $2p_{3/2}$ of Ni^{2+} (854.12 eV) and $2p_{1/2}$ of Ni^{2+} (871.71 eV) ions, as well as the corresponding satellite peaks at 859.83 and 876.71 eV. The Co(2p) spectrum shown in Figure 2(c) could be divided into peaks, which can be assigned to $2p_{3/2}$ of Co^{2+} (779.11 eV) and $2p_{1/2}$ of Co^{2+} (794.81 eV) ions, as well as the corresponding satellite peaks at 783.87 and 799.87 eV that arise from Co^{2+} ions. The O(1s) spectra shown in Figure 5.2(d) represent two binding energies at 530.23 and 528.58 eV for different C=O and C−O bond stretchings. [17]

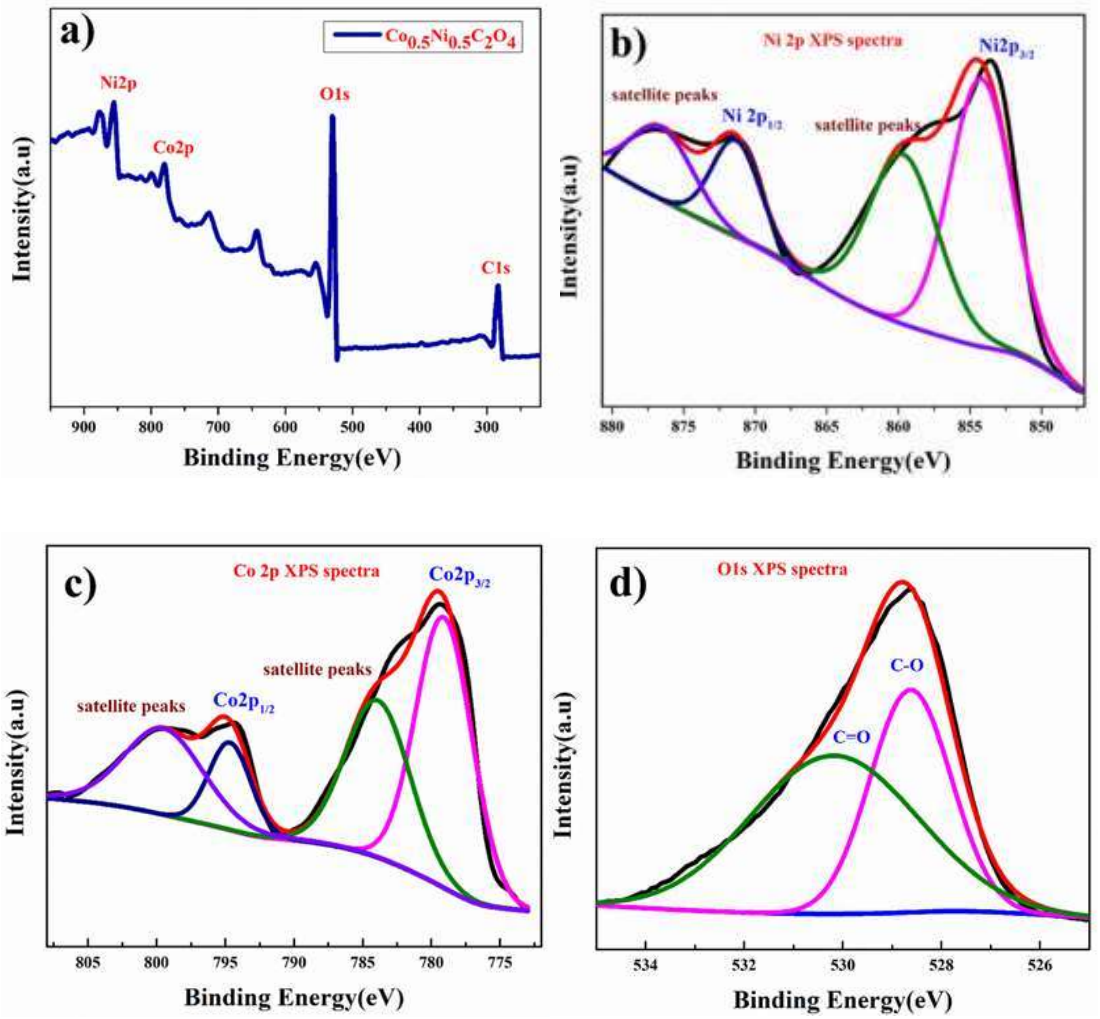

Figure 5.2: XPS plot of (a) full survey $Co_{0.5}Ni_{0.5}C_2O_4$, (b) Ni (2p) spectra, (c) Co 2p spectra, and (d) O (1s) spectra.

5.5 SEM/EDX Study

The SEM image shown in Figure 5.3(a) displays the particle distribution and morphology of the $Co_{0.5}Ni_{0.5}C_2O_4$ powder sample. It shows a spongy-like arrangement. The inset (energy dispersive X-ray analysis) image represents the elemental analysis of anhydrous $Co_{0.5}Ni_{0.5}C_2O_4$. To determine the diameter of grains, ImageJ software was used. Agglomerated sub-micron size grains are visible in the SEM image. TEM shows atomic arrangements at localized regions within the sample shown in Figure 5.3(b). The inset image

represents FFT (fast Furrier transformation) and inverse FFT, and the calculated d spacing was found to be 0.227 nm, which matches the (110) plane of $Co_{0.5}Ni_{0.5}C_2O_4$.

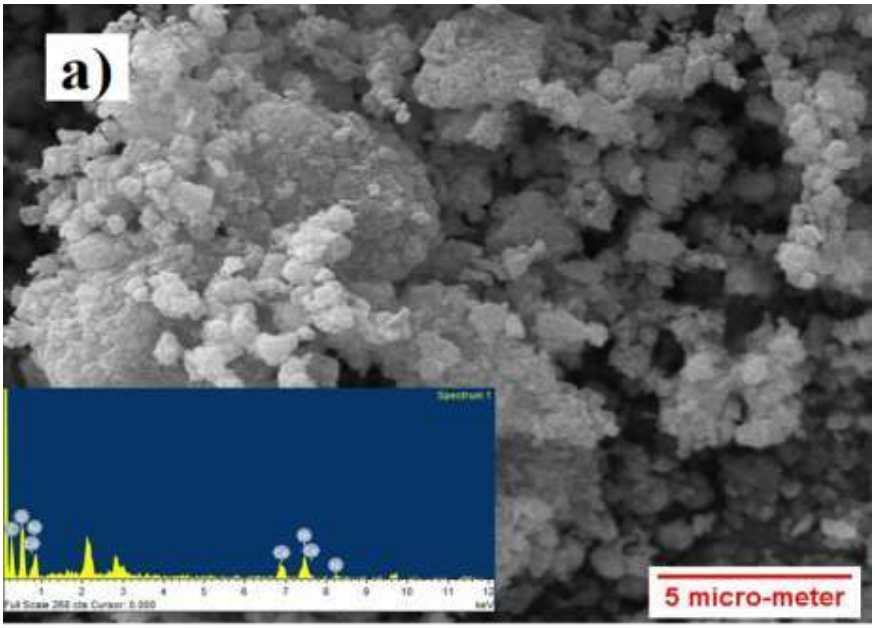

Figure 5.3: (a) SEM image showing the morphology and particle size distribution of anhydrous $Ni_{0.5}Co_{0.5}C_2O_4$ powder; inset shows the EDX image of anhydrous $Co_{0.5}Ni_{0.5}C_2O_4$.

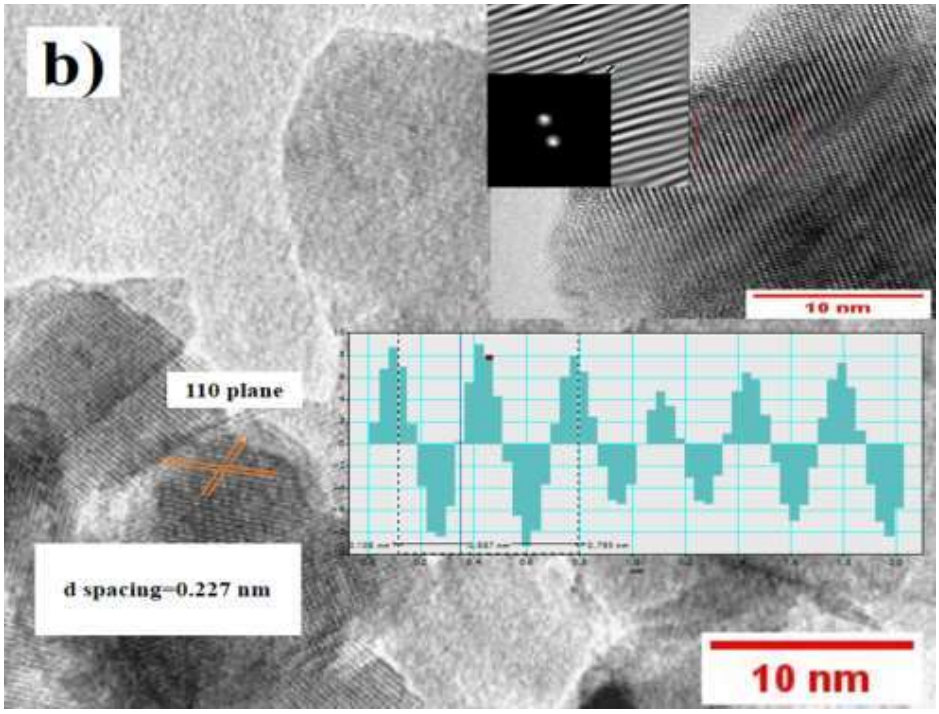

Figure 5.3: (b) TEM image at localized regions; inset shows enlarged lattice fringes (with FFT and inverse FFT) and also (110) plane d spacing of porous anhydrous $Co_{0.5}Ni_{0.5}C_2O$

5.6 Electrochemical Studies:

Electrochemical performance of $Co_{0.5}Ni_{0.5}C_2O_4{\cdot}2H_2O$ and porous anhydrous $Co_{0.5}Ni_{0.5}C_2O_4$ as the working electrode was characterized using a three-electrode system, where $Co_{0.5}Ni_{0.5}C_2O4{\cdot}2H_2O$ and porous anhydrous $Co_{0.5}Ni_{0.5}C_2O_4$ act as working electrodes, saturated Hg/HgO (1 M KOH) as a reference electrode, and a platinum wire as a counter electrode in 2 M KOH as an electrolyte. The charge storage behavior of $Co_{0.5}Ni_{0.5}C_2O4{\cdot}2H_2O$ and porous anhydrous $Co_{0.5}Ni_{0.5}C_2O_4$ was characterized using cyclic voltammetry (CV) curves in the potential range of 0−0.6 V. Figure 4a represents the CV curve of $Co_{0.5}Ni_{0.5}C_2O4{\cdot}2H_2O$. The nature of the curve explains the pseudocapacitive behavior coupled with surface redox (electrosorption). The CV curve of highly porous anhydrous $Ni_{0.5}Co_{0.5}C_2O_4$ shown in Figure 4b shows that pseudocapacitive storage followed intercalative association with surface redox.[18] Redox peaks originated due to the reversible transformation between Co^{2+} to Co^{3+} and Ni^{2+} to Ni^{3+} through electrosorption (redox) of OH^- ions. [18]

$$2Co_{0.5}(II)Ni_{0.5}(II)C_2O_4.2H_2O + 2OH^-_{sol} \longleftrightarrow Ni(III)(OH^-)Co(III)(OH^-)C_2O_4.2H_2O + 2e^- \quad (5.5)$$

$$2Co_{0.5}(II)Ni_{0.5}(II)CO_4\,C_2O_4 + 2OH^-_{sol} \longleftrightarrow Co(III)(OH^-)\,Ni_{0.5}(III)(OH^-)\,C_2O_4 + 2e^- \quad (5.6)$$

From the CV curve, the specific capacitance C (F/g) can also be calculated as one of the significant parameters to understand the electrochemical performance of the working electrode.[19]

$$Csp = \frac{\int i\,(V)\,dV}{mV\vartheta} \quad (5.7)$$

Where '*m*' is the mass of active material in the electrode (g), '*V*' is the potential window (V) and 'ϑ' is the scan rate (mV/s).

The specific capacitances of $Co_{0.5}Ni_{0.5}C_2O_4 \cdot 2H_2O$ and anhydrous $Co_{0.5}Ni_{0.5}C_2O_4$ were calculated using equation (5.7), and capacitance was found to be close to 671 and 1993 F/g at 1 mV/s, respectively. The highly porous anhydrous $Co_{0.5}Ni_{0.5}C_2O_4$ attains higher charge storage, resulting in much higher capacity compared to hydrated $Co_{0.5}Ni_{0.5}C_2O_4 \cdot 2H_2O$. In the voltage window of 0.6 V, the theoretical capacity of $Co_{0.5}Ni_{0.5}C_2O_4 \cdot 2H_2O$ and anhydrous $Co_{0.5}Ni_{0.5}C_2O_4$ will be 879.55 F/g and 1096 F/g, respectively, with 1e−/OH− charge transfer coupled with reversible intercalation/de-intercalation of OH− ions. This suggests that there is at least a transfer/exchange of 0/76e^-/OH^- per $Co_{0.5}Ni_{0.5}C_2O4 \cdot 2H_2O$ and 1.82e^-/OH^- per $Ni_{0.5}Co_{0.5}C_2O_4$ molecule, suggesting the participation of both $Ni^{2+/3+}$ and $Co^{2+/3+}$ redox couples in charge storage. The redox reaction for the high capacitance of $Co_{0.5}Ni_{0.5}C_2O4 \cdot 2H_2O$ can be represented as

$$Co_{0.5}^{2+}\ Ni_{0.5}^{2+}C_2O_4.2H_2O + 0.76OH^- \longleftrightarrow Co_{0.38}^{3+}\ Co_{0.12}^{2+}\ \ Ni_{0.38}^{3+}Ni_{0.12}^{2+}\ C_2O_4.2H_2O\ (OH^-)_{0.76} \quad (5.7)$$

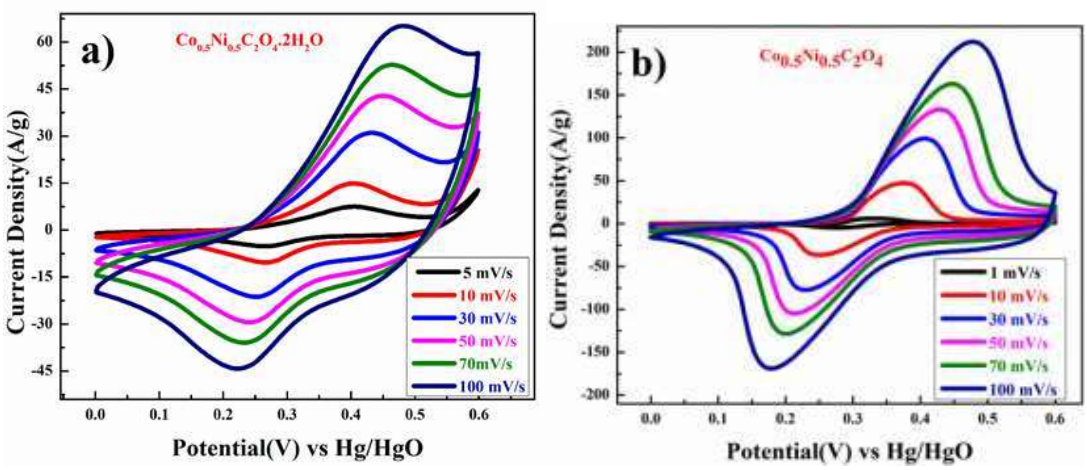

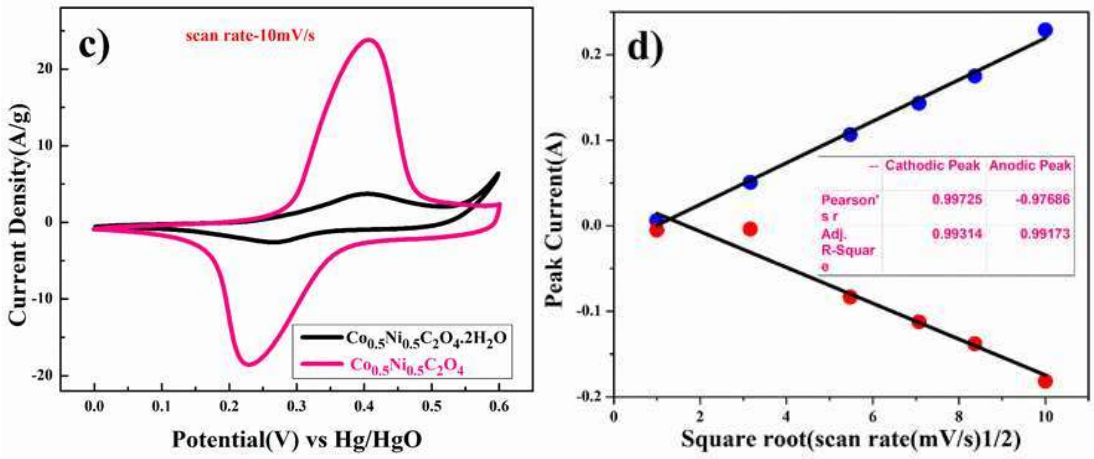

Figure 5.4: (a) Cyclic voltammetry of $Ni_{0.5}Co_{0.5}C_2O_4$.$2H_2O$, (b) cyclic voltammetry of porous anhydrous $Ni_{0.5}Co_{0.5}C_2O_4$, (c) comparative cyclic voltammetry curves for $Ni_{0.5}Co_{0.5}C_2O_4$.$2H_2O$ and $Ni_{0.5}Co_{0.5}C_2O_4$ electrodes at 10 mV/s, and (d) plot of log (peak current vs square root of the scan rate for porous anhydrous $Ni_{0.5}Co_{0.5}C_2O_4$).

As given in equation (5.8) the capacitance of $Co_{0.5}Ni_{0.5}C_2O_4$ can be represented as a combination of redox reaction as well as double layer formation as electron transfer is more than 1.

$$Co^{2+}_{0.5}\,Ni^{2+}_{0.5}C_2O_4 + xOH^- + 1.82\text{-}xKOH \rightarrow Co^{3+}_{x}Co^{2+}_{0.5-x}\,Ni^{3+}_{x}Ni^{2+}_{0.5-x}C_2O_4(OH^-)_{1.82} \qquad (5.8)$$

The value of x can vary with scan rates, and the detailed electrochemistry $Co_{0.5}Ni_{0.5}C_2O_4$ is described later to understand the charge storage mechanism of the electrode. We believe that as $Co_{0.5}Ni_{0.5}C_2O_4$ can easily accommodate two structural water molecules to form $Co_{0.5}Ni_{0.5}C_2O4{\cdot}2H_2O$, the anhydrous $Co_{0.5}Ni_{0.5}C_2O_4$ accommodate high charge transfer ($1.82e^-/OH^-$) coupled with double layer capacitance formation to result in very high capacity for the anhydrous $Co_{0.5}Ni_{0.5}C_2O_4$ electrode. Figure 5.4(c) shows a comparative plot of the CV curve of $Co_{0.5}Ni_{0.5}C_2O_4{\cdot}2H_2O$ and $Co_{0.5}Ni_{0.5}C_2O_4$ at a scan rate of 10 mV/s. The plot reveals that there are two different types of redox phenomena occurring in the charge storage process; $Co_{0.5}Ni_{0.5}C_2O_4{\cdot}2H_2O$ follows surface redox and $Co_{0.5}Ni_{0.5}C_2O_4$ surface redox with intercalation and double layer formation.[20]

As the anhydrous $Co_{0.5}Ni_{0.5}C_2O_4$ electrode showed much superior pseudocapacitive storage, we focused our study mainly on the anhydrous $Co_{0.5}Ni_{0.5}C_2O_4$ only. Figure 5.4(d) shows the linear relation between anodic and cathodic peak current with respect to the square root of scan rate and indicates that anhydrous $Co_{0.5}Ni_{0.5}C_2O_4$ undergoes the semi-infinite diffusion-controlled process. Furthermore, the kinetics of the electrode can be understood by determining the diffusion coefficient. The diffusion coefficient for the electrode was determined using the Randles−Sevick equation.[21]

$$i_p = 2.686 \times 10^5 \times n^{3/2} A D^{1/2} C_o v^{1/2} \qquad (5.9)$$

where ip is peak current (A), n is the number of electrons transferred in the redox event (usually 1), A is the electrode area in cm^2, D is the diffusion coefficient in cm^2/s, Co is the OH− ion concentration in mol/cm3, and ν is the scan rate in V/s. According to the equation, the diffusion coefficient of $Co_{0.5}Ni_{0.5}C_2O_4$ was calculated to be 1.916 × 10−11 cm^2/s for oxidation and 4.8931 × 10−11 cm^2/s for reduction.

To further estimate the qualitative contribution of the different charge storage kinetics/mechanisms of the electrode, the power law equation is given in equation (5.10) was utilized.

$$\boldsymbol{i = a v^b} \qquad (5.10)$$

where a and b are adjustable values, i is the current (A), and ν is the scan rate (V/s). The value of b lies between 0.5 and 1, b = 0.5 stands for the semi-infinite diffusion control reaction, that is, battery-type intercalative behavior, while b = 1 stands for the surface control reaction or electrosorption. Figure 5.5(a) shows the slopes (b value) of the corresponding log [peak current (ip) versus log(v) plots]. The b-values of oxidative and reductive current were found to be 0.58 and 0.57, respectively, indicating the dominance of semi-infinite diffusion-controlled intercalative processes resulting in battery-type supercapacitor behavior during the electrochemical reaction.[22] Figure 5.5(b) shows the voltammetry sweep rate dependence

that can distinguish quantitatively the capacitive contribution to the current response. The current response at a fixed potential is the contribution of two separate mechanisms, surface capacitive effects, and diffusion-controlled insertion or intercalation.

$$i(\upsilon) = k_1 v + k_2 v^{\frac{1}{2}} \qquad (5.11)$$

For better understanding, eq 11 was modified as

$$\frac{i(\upsilon)}{\upsilon^{\frac{1}{2}}} = \frac{k_1}{\upsilon^{\frac{1}{2}}} + k_2 \qquad (5.12)$$

In equation (5.11), $k_1\upsilon$ and $k_2\upsilon^{1/2}$ represent the current contributions from the surface capacitive process and the diffusion-controlled intercalation process, respectively. Thus, after the determination of k_1 and k_2, we can quantify their contribution to the current density at specific potentials. [23] k_1 and k_2 were determined by obtaining the slope and intercept of the y-axis from the linear fit. The representative curve ($i(V)/\upsilon^{1/2}$ vs $\upsilon^{1/2}$) shown in Figure 5.5(c) represents the contribution of surface capacitance and diffusion-controlled intercalation at different scan rates. Figure 5.5(d) represents a specific contribution at a 10 mV/s scan rate, and the contribution of surface capacitance or electrosorption was found to be 58% and that of diffusion-controlled intercalation was found to be close to 42%.

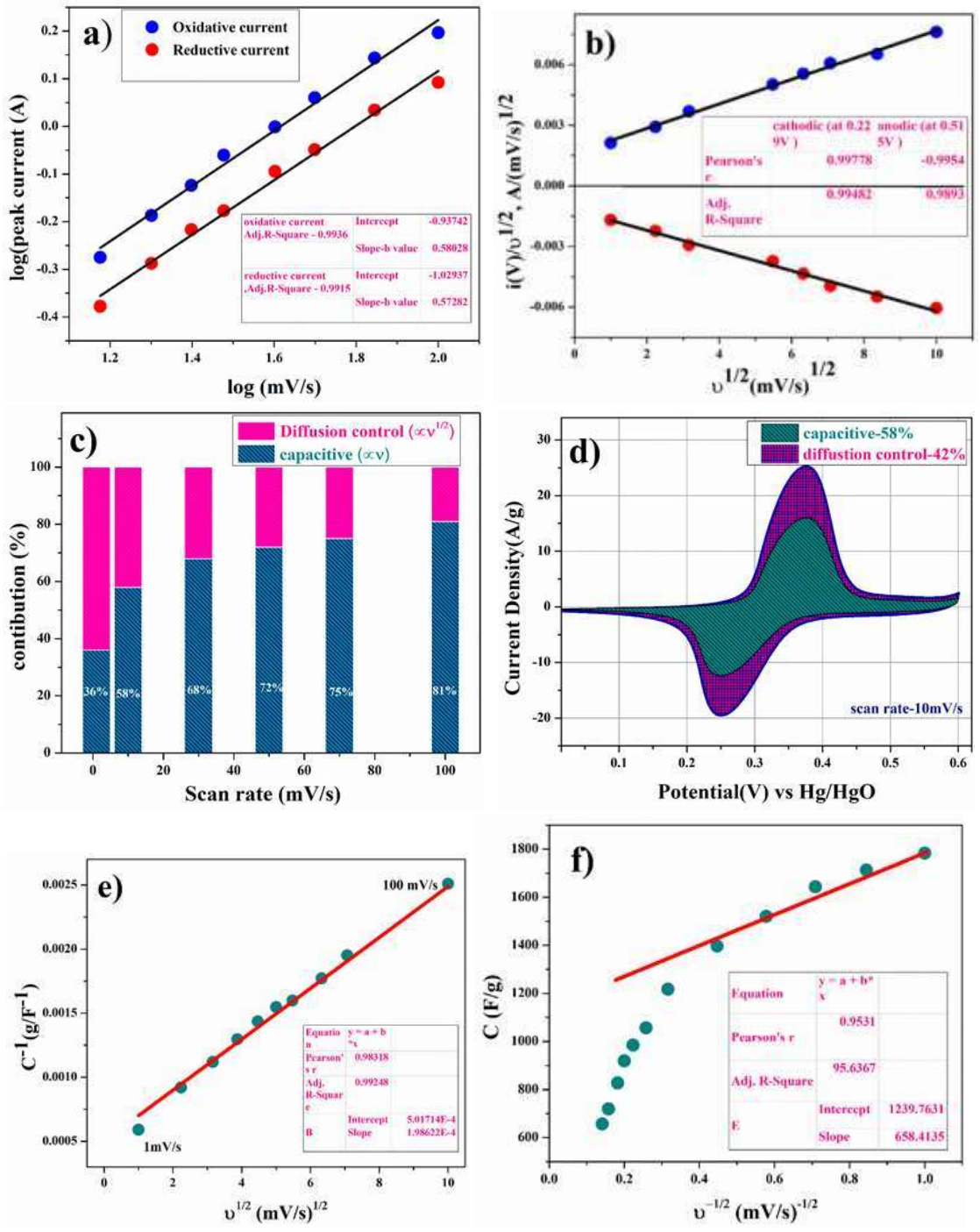

Figure 5.5: Electrodynamic characteristics of the $Co_{0.5}Ni_{0.5}C_2O_4$ electrode; (a) plot of the linear relationship between log (peak current) and log (scan rate) at two different scan rate regions, (b) plot of the power law of the charged state at a potential and discharged state at a potential, (c) contribution of diffusive and capacitive contribution at different scan rates, (d) analysis of kinetic contribution at 10 mV/s, and (e, f) show Trasatti plot at different scan rates.

According to Trassati, the total specific capacitance is the sum of the inner and outer surface capacitance of the electrode. It can be expressed as

$$C_{total}=C_{in}+C_{out}\ (F/g) \qquad (5.13)$$

The specific capacitance contributed from the inner and outer surface of the electrode is dependent on scan rates.[24] Figure 5.5(e) shows the linear fit C^{-1} versus $\upsilon^{1/2}$ at different scan rates, and the y-intercept represents the amount of total charge storage or capacitance of the electrode. Figure 5.5(f) shows the linear fit C versus $\upsilon^{-1/2}$, and the y-intercept represents the outer surface charge storage or capacitance of the electrode. After calculating the y-intercept value applied on the Trassati plot, the total capacitance value (C_{total}) was found to be 1993F/g, Cin was found to be 754 F/g (38% of the total capacitance value), and Cout was found to be 1239 F/g (62% of the total capacitance value).

Galvanostatic experiments were carried out to get a more accurate capacity assessment of $Co_{0.5}Ni_{0.5}C_2O_4{\cdot}2H_2O$ and highly porous anhydrous $Co_{0.5}Ni_{0.5}C_2O_4$ electrodes. From the charge/discharge curve, the specific capacitance of the electrode was calculated using equation (5.14).[19]

$$Csp = \frac{I\Delta t}{m\Delta V} \qquad (5.14)$$

where I is the discharge current (A), Δt is the discharge time (s), m is the mass of the active material in the electrode (g), and ΔV is the potential change during discharge (V). Figure 5.6(a) depicts the specific capacitances of $Co_{0.5}Ni_{0.5}C_2O_4{\cdot}2H_2O$, and the values were found to be 810, 350, and 216 F/g at current densities of 1, 2, and 5A/g, respectively. Figure 6(b) shows the specific capacitances of the highly porous anhydrous $Co_{0.5}Ni_{0.5}C_2O_4$ electrode, and the values were found to be 2409, 2396, 2126, 1226, and 1083 F/g at current densities of 0.5, 1, 2, 5, and 10 A/g, respectively. It has been observed that with an increase in current density, there was a decrease in the specific capacitance of the electrode. In the desired range of current density, the specific capacitance decreases to 55% of its initial value. Figure 6c shows

the capacitance value of the cycle number with different currents of the highly porous anhydrous $Co_{0.5}Ni_{0.5}C_2O_4$ electrode. Figure 5.6(d) exhibits the excellent long-term cyclic stability of highly porous anhydrous $Co_{0.5}Ni_{0.5}C_2O_4$ electrodes at 10 A/g for 5000 cycles. 87% capacity retention reflects that the specific capacitance of the electrode did not change much from the initial capacitance after 5000 cycles. The columbic efficiency (η = td/tc) of the electrode was 94.8% after 5000 cycles of charge/discharge, which reveals the high reversibility of the highly porous anhydrous $Co_{0.5}Ni_{0.5}C_2O_4$ electrode. In addition to electrochemical stability, we performed AC electrochemical impedance spectroscopy (EIS) at 10 mV, as shown in the Nyquist plot in Figure 5.6(e), in the frequency range of 1 MHz to 0.1 Hz. The specific impedance contribution was attributed to the impedance distributions over electric series resistance (Rs), charge transfer resistance (Rct), and Warburg impedance (Rw). Higher frequency resistance was found for $Co_{0.5}Ni_{0.5}C_2O_4 \cdot 2H_2O$ than porous anhydrous $Co_{0.5}Ni_{0.5}C_2O_4$ electrodes, as the intercept of the EIS spectra on the real axis was found to be at 1.43 and 0.8 Ω, respectively, indicating very small internal resistance for the anhydrous $Co_{0.5}Ni_{0.5}C_2O_4$ electrode. The small semicircle in the high-frequency region shows the fast charge transport between the electrode and electrolyte. Lower frequency data represent the Warburg diffusion resistance for the samples. The straight line in the low-frequency region for the porous anhydrous $Co_{0.5}Ni_{0.5}C_2O_4$ electrode is close to a 90° angle [very close to $-Z''(\Omega)$ axis], and the horizontal line represents the characteristic of more pseudocapacitance behavior of the electrode. The straight line in the low-frequency region also represents fast OH^- ion diffusion in the porous structure.[25]

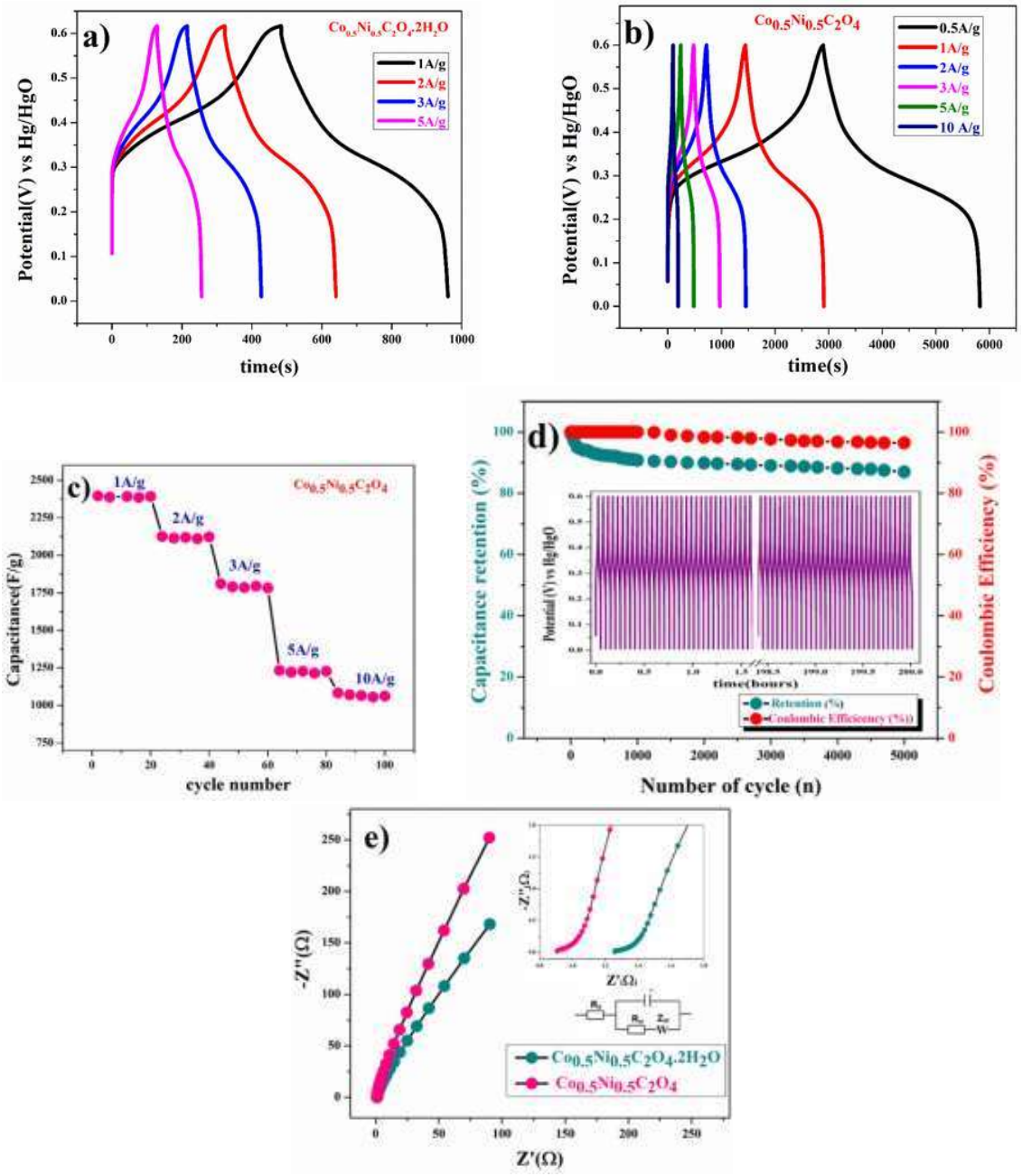

Figure 5.6: (a) Charge/discharge curve of $Co_{0.5}Ni_{0.5}C_2O4{\cdot}2H_2O$, (b) charge/discharge curve of porous anhydrous $Co_{0.5}Ni_{0.5}C_2O_4$, (c) capacitance performance of porous anhydrous $Co_{0.5}Ni_{0.5}C_2O_4$ at different constant current rates, (d) capacitance retention and Coulombic efficiency porous anhydrous $Co_{0.5}Ni_{0.5}C_2O_4$, and (e) EIS plot and enlarged (zoom) view of the EIS plot of $Co_{0.5}Ni_{0.5}C_2O4{\cdot}2H_2O$ and porous anhydrous $Co_{0.5}Ni_{0.5}C_2O_4$ electrode at 10 mV (AC).

5.7 Two electrode test:

To understand the real charge storage behavior of the porous anhydrous $Co_{0.5}Ni_{0.5}C_2O_4$ sample relative to AC (activated carbon), two electrode measurements have been conducted in 2 M KOH. To determine the maximum specific capacitance during the full test, the storage capacity of positive and negative electrodes needs to be balanced as per the following equation:

$$\frac{1}{C_{total}} = \frac{1}{C_{positive}} + \frac{1}{C_{negative}} \quad (5.15)$$

For balancing the charge storage capacity of the cell, the mass ratio (m^+/m^-) of positive and negative electrode material was measured using the following equation:

$$\frac{m^+}{m^-} = \frac{C_- \times \Delta E_-}{C_+ \times \Delta E_+} \quad (5.16)$$

$m^+, m^-, C_+, C_-, \Delta E_+, \Delta E_-$ are mass, specific capacitance, and potential window of positive and negative electrodes estimated by three-electrode measurement respectively. [26-27]

Figure 5.7(a) shows CV curves at a 10 mV/s scan rate, where AC (activate carbon) was used as the negative electrode and porous anhydrous $Co_{0.5}Ni_{0.5}C_2O_4$ was used as the positive electrode. The calculated mass ratio (m^+/m^-) was found to be 1: 5.3 for the asymmetric cell, and the weight of the active material was measured to be 4.41 mg (excluding the weight of acetylene black and PVDF). Figure 7b demonstrates the CV curve of porous anhydrous $Co_{0.5}Ni_{0.5}C_2O_4$ //AC two-electrode ASCs [asymmetry supercapacitor cell at scan rates of 1−100 mV/s in this potential window (1.6 V)]. Figure 5.7(c) subsequently shows the galvanostatic charge/discharge curve, and the capacitance values were calculated by equation (5.14). Capacitance values were found to be 796, 515, 453, 421, and 211F/g at current densities of 1, 2, 3, 5, and 10 A/g, respectively. Figure 5.7(d) shows the EIS plot (Nyquist) in the frequency range of 1 MHz to 0.1 Hz at 10 mV/s, confirming the retention of the electronic structure and resistance of the full cell (anhydrous $Co_{0.5}Ni_{0.5}C_2O_4$ //AC), as the

impedance of the material decreases after completion of 2500 cycles compared to the first cycle.

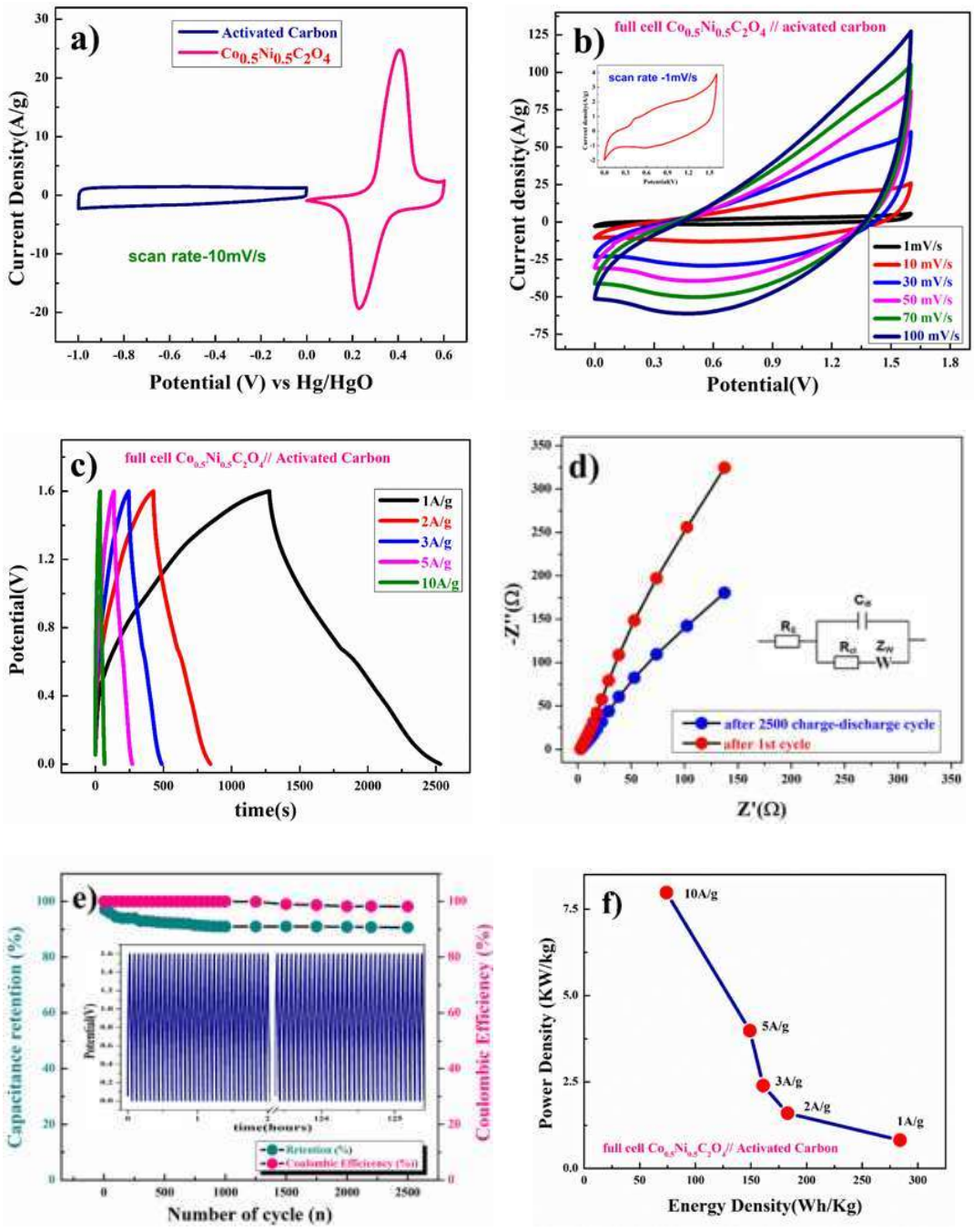

Figure 5.7: (a) Representative CV for activated carbon (AC) and porous anhydrous $Co_{0.5}Ni_{0.5}C_2O_4$ at 10 mV/s, (b) plot for activated carbon and the porous anhydrous $Co_{0.5}Ni_{0.5}C_2O_4$ cell in ASC mode CV at different scan rates, (c) charge/discharge at different current rates, (d) EIS at 10 mV (AC), (e) capacitance retention and columbic efficiency, and (f) power density and energy density of two electrode cells in ASC mode.

Figure 5.7(e) shows the columbic efficiency of the two-electrode cell, and the cell has lost only 3% efficiency after the completion of 2500 cycles with higher capacity retention (90.7%) of its initial value after 2500 cycles. Specific energy and specific power of asymmetric capacitors were calculated using the following equations

$$E(Wh/kg) = \frac{1}{2}\frac{C_{ASCs}}{3.6}V^2 \quad (5.17)$$

$$P(W/kg) = \frac{E*3600}{t_{dis}} \quad (5.18)$$

where C_{ASCs} is specific capacitance, V is operating voltage and t_{dis} is discharge time.[27] Figure 5.7(f) shows the plot of specific energy versus specific power with different constant current rates. Resultant values confirm the highest specific energy equivalent to 283 W h/kg at 1 A/g current density with specific power equivalent to ~817 W/kg. The maximum specific power of ~7981 W/kg was obtained when specific energy was reduced to ~75.37 W h/kg at 10 A/g of current density. The capacitances of bulk/pristine transition-metal oxalate-based pseudocapacitors are summarized in Table5.1 and are similar to those of anhydrous $Co_{0.5}Ni_{0.5}C_2O_4$ electrodes. The charge storage pseudocapacitive behavior of the $Co_{0.5}Ni_{0.5}C_2O_4$ electrode and the capacitance value are comparable or superior to that of most bulk/pristine transition-metal oxalate-based pseudocapacitors reported to date.[16,28-31] We believe that the controlled release of the water molecule from hydrated transition oxalate molecule results in anhydrous porous structured material that can accommodate the storage of two molecules/ions (OH^-) (intercalation couple with double layer capacitance) over the electrode is the key step in developing superior capacitance or charge storage materials.[32]

Material	Morphology	Capacitance (F g^{-1})	Operating potential (V)	Electrolyte	Reference
CoC_2O_4	Thin sheet	1269 at 6 A g^{-1}	0 to 0.5	6 M KOH	28
$Co_{0.5}Mn_{0.4}Ni_{0.1}C_2O_4.nH_2O$	Micro polyhedrons	990 at 0.6 A g^{-1}	0 to 0.4	3 M KOH	29
$CoC_2O_4.2H_2O$	2D porous thin sheets	1.631 F cm^{-2} at 1.20 mA cm^{-1}	0 to 0.4	6 M KOH	30
NiC_2O_4	2D thin sheet	2835 F g^{-1} at	0 to 0.4	6 M KOH	31
$Ni_{0.55}Co_{0.45}C_2O_4$	Micro-cuboid	562 C g^{-1} 1A g^{-1}	0 to 0.6	6 M KOH	16
MnC_2O_4/GO	Olive-like	122 F g^{-1} at 0.5 A g^{-1}	-0.1 to 0.55	6 M KOH	22
$Co_{0.5}Ni_{0.5}C_2O_4 \cdot 2H_2O$ anhydrous	Nanoflakes	810 F/g at 1 A/g	0 to 0.6	2 M KOH	Present work
$Co_{0.5}Ni_{0.5}C_2O_4$	Nanoflakes	2409 F/g at 1 A/g and 1993 F/g at 1 mV/s	0 to 0.6	2 M KOH	Present work

Table 5.1:comparison of capacitive performances of different oxalate based electrodes

5.8 Conclusion

In summary, porous anhydrous $Co_{0.5}Ni_{0.5}C_2O_4$ was successfully synthesized using a two-step process; first, $Co_{0.5}Ni_{0.5}C_2O4 \cdot 2H_2O$ was synthesized by the co-precipitation method in an aqueous medium, and then $Co_{0.5}Ni_{0.5}C_2O4 \cdot 2H_2O$ was heated at 230 °C for 5 h, which resulted in porous anhydrous $Co_{0.5}Ni_{0.5}C_2O_4$. The anhydrous $Co_{0.5}Ni_{0.5}C_2O_4$ electrode showed a highly pseudocapacitive performance with a specific capacitance of 2396 F/g at a current density of 1 A/g and excellent cyclic stability. Predominant intercalative mechanism seems to operate behind high charge storage capacity of the materials as intercalative (inner) and surface (outer) charges stored by porous anhydrous $Co_{0.5}Ni_{0.5}C_2O_4$ were close to high 38 and 62%, respectively. The porous anhydrous $Co_{0.5}Ni_{0.5}C_2O_4$ //AC full cell resulted in 283 W h/kg of maximum specific energy with a specific power equivalent to 817 W/kg in the voltage window of 1.6 V in the 2 M KOH electrolyte at a 1 A/g current rate. These results confirm

that porous anhydrous $Co_{0.5}Ni_{0.5}C_2O_4$ can act as a potential pseudocapacitive electrode for large-scale energy storage applications.

References:

1. Devaraj, S.; Munichandraiah, N. Effect of Crystallographic Structure of MnO_2 on Its Electrochemical Capacitance Properties. J. Phys. Chem. C 2008, 112, 4406−4417.
2. Liu, K. C.; Anderson, M. A. Porous Nickel Oxide/Nickel Films for Electrochemical Capacitors. J. Electrochem. Soc. 1996, 143, 124−130.
3. (a) Lee, H. Y.; Goodenough, J. B. Ideal Supercapacitor Behavior of Amorphous $V_2O_5{\cdot}nH_2O$ in Potassium Chloride (KCl) Aqueous Solution. J. Solid State Chem. 1999, 148, 81−84. (b) Kamila, S.; Mane, P.; Mohanty, R. I.; Chakraborty, B.; Jena, B. K. Supercapacitor properties of $V10O14(OH)_2$ and reduced graphene oxide hybrids: Experimental and theoretical insights. Electrochim. Acta 2021, 399, 139357. (c) Kamila, S.; Chakraborty, B.; Basu, S.; Jena, B. K. Combined Experimental and Theoretical Insights into Energy Storage Applications of a VO_2(D)-Graphene Hybrid. J. Phys. Chem. C 2019, 123, 24280−24288.
4. Gao, Y.; Chen, S.; Cao, D.; Wang, G.; Yin, J. Electrochemical capacitance of Co_3O_4 nanowire arrays supported on nickel foam. J. Power Sources 2010, 195, 1757−1760.
5. Xia, X.-H.; Tu, J.-P.; Wang, X.-L.; Gu, C.-D.; Zhao, X.-B. Mesoporous Co_3O_4 monolayer hollow-sphere array as electrochemical pseudocapacitor material. Chem. Commun. 2011, 47, 5786−5788.
6. Wang, S.-Y.; Ho, K.-C.; Kuo, S.-L.; Wu, N.-L. Investigation on Capacitance Mechanisms of Fe[sub 3]O[sub 4] Electrochemical Capacitors. J. Electrochem. Soc. 2006, 153, A75−A80.
7. (a) Liu, X. Y.; Zhang, Y. Q.; Xia, X. H.; Shi, S. J.; Lu, Y.; Wang, X. L.; Gu, C. D.; Tu, J. P. Self-assembled porous $NiCo_2O_4$ heterostructure array for electrochemical capacitor. J. Power Sources 2013, 239, 157−163. (b) Samantara, A. K.; Kamila, S.; Ghosh, A.; Jena, B. K. Highly ordered 1D $NiCo_2O_4$ nanorods on graphene: An

efficient dual-functional hybrid materials for electrochemical energy conversion and storage applications. Electrochim. Acta 2018, 263, 147−157.

8. Jabeen, N.; Xia, Q.; Savilov, S. V.; Aldoshin, S. M.; Yu, Y.; Xia, H. Enhanced Pseudocapacitive Performance of α-MnO_2 by Cation Preinsertion. ACS Appl. Mater. Interfaces 2016, 8, 33732−33740.
9. (a) Singh, A. K.; Jaiswal, P.; Singh, P. A Review on Transitionmetal Oxalate Based Electrode for Supercapacitors. IOP Conf. Ser.: Mater. Sci. Eng. 2021, 1166, 012032. (b) Mishra, N. K.; Mondal, R.; Singh, P. Synthesis, characterizations and electrochemical performances of anhydrous CoC_2O_4 nanorods for pseudocapacitive energy storage applications. RSC Adv. 2021, 11, 33926−33937.
10. (a) Gao, Y.; Wu, J.; Zhang, W.; Tan, Y.; Gao, J.; Zhao, J.; Tang, B. Synthesis of nickel oxalate/zeolitic imidazolate framework-67 (NiC_2O_4/ZIF-67) as a supercapacitor electrode. New J. Chem. 2015, 39, 94−97. (b) Zhang, Y.-Z.; Zhao, J.; Xia, J.; Wang, L.; Lai, W.-Y.; Pang, H.; Huang, W. Room temperature synthesis of cobalt manganese- nickel oxalates micropolyhedrons for high performance flexible electrochemical energy storage device. Sci. Rep. 2015, 5, 8536.
11. Saraf, M.; Rajak, R.; Mobin, S. M. A fascinating multitasking Cu-MOF/rGO hybrid for high performance supercapacitors and highly sensitive and selective electrochemical nitrite sensors. J. Mater. Chem. A 2016, 4, 16432−16445.
12. Han, X.; Tao, K.; Wang, D.; Han, L. Design of a porous cobalt sulfide nanosheet array on Ni foam from zeolitic imidazolate frameworks as an advanced electrode for supercapacitors. Nanoscale 2018, 10, 2735−2741.
13. Yang, J.; Xiong, P.; Zheng, C.; Qiu, H.; Wei, M. Metal-organic frameworks: a new promising class of materials for a high performance supercapacitor electrode. J. Mater. Chem. A 2014, 2, 16640−16644.

14. Wang, J.; Yang, L.; Fu, Y.; Yin, P.; Guan, X.; Wang, G. Delicate control of crystallographic Cu_2O derived Ni-Co amorphous double hydroxide nanocages for high-performance hybrid supercapacitors: an experimental and computational investigation. Nanoscale 2021, 13, 8562−8574.
15. Małecka, B.; Małecki, A.; Drożdż-Cieśla, E.; Tortet, L.; Llewellyn, P.; Rouquerol, F. Some aspects of thermal decomposition of $NiC_2O_4{\cdot}2H_2O$. Thermochim. Acta 2007, 466, 57−62.
16. Wang, L.; Zhang, R.; Jiang, Y.; Tian, H.; Tan, Y.; Zhu, K.; Yu, Z.; Li, W. Interfacial synthesis of micro-cuboid $Ni_{0.55}Co_{0.45}C_2O_4$ solid solution with enhanced electrochemical performance for hybrid supercapacitors. Nanoscale 2019, 11, 13894−13902.
17. Chenakin, S.; Kruse, N. XPS characterization of transition metal oxalates. Appl. Surf. Sci. 2020, 515, 146041.
18. Evanko, B.; Boettcher, S. W.; Yoo, S. J.; Stucky, G. D. Redox- Enhanced Electrochemical Capacitors: Status, Opportunity, and Best Practices for Performance Evaluation. ACS Energy Lett. 2017, 2, 2581−2590.
19. Shi, F.; Li, L.; Wang, X.-L.; Gu, C.-D.; Tu, J.-P. Metal oxide/ hydroxide-based materials for supercapacitors. RSC Adv. 2014, 4, 41910−41921.
20. Jha, M. K.; Babu, B.; Parker, B. J.; Surendran, V.; Cameron, N. R.; Shaijumon, M. M.; Subramaniam, C. Hierarchically engineered nanocarbon florets as bifunctional electrode materials for adsorptive and intercalative energy storage. ACS Appl. Mater. Interfaces 2020, 12, 42669−42677.
21. Hanzu, I.; Djenizian, T.; Knauth, P. Electrical and Point Defect Properties of TiO_2 Nanotubes Fabricated by Electrochemical Anodization. J. Phys. Chem. C 2011, 115, 5989−5996.

22. Augustyn, V.; Come, J.; Lowe, M. A.; Kim, J. W.; Taberna, P.- L.; Tolbert, S. H.; Abruña, H. D.; Simon, P.; Dunn, B. High-rate electrochemical energy storage through Li+ intercalation pseudocapacitance. Nat. Mater. 2013, 12, 518−522.
23. Kim, H.-S.; Cook, J. B.; Lin, H.; Ko, J. S.; Tolbert, S. H.; Ozolins, V.; Dunn, B. Oxygen vacancies enhance pseudocapacitive charge storage properties of MoO_{3-x}. Nat. Mater. 2017, 16, 454− 460.
24. Ren, W.; Chen, X.; Zhao, C. Ultrafast Aqueous Potassium-Ion Batteries Cathode for Stable Intermittent Grid-Scale Energy Storage. Adv. Energy Mater. 2018, 8, 1801413.
25. Basiricò, L.; Lanzara, G. Moving towards high-power, high frequency and low-resistance CNT supercapacitors by tuning the CNT length, axial deformation and contact resistance. Nanotechnology 2012, 23, 305401.
26. Subramani, K.; Sudhan, N.; Divya, R.; Sathish, M. All-solid state asymmetric supercapacitors based on cobalt hexacyanoferrate derived CoS and activated carbon. RSC Adv. 2017, 7, 6648−6659.
27. Hu, N.; Gong, W. H.; Huang, L.; Shen, P. K. Ultrahigh energy density asymmetric electrochemical capacitors based on flower-like ZnO/Co3O4 nanobundle arrays and stereotaxically constricted graphene. J. Mater. Chem. A 2019, 7, 1273−1280.
28. Cheng, G.; Si, C.; Zhang, J.; Wang, Y.; Yang, W.; Dong, C.; Zhang, Z. Facile fabrication of cobalt oxalate nanostructures with superior specific capacitance and super-long cycling stability. J. Power Sources 2016, 312, 184−191.
29. Zhang, Y.-Z.; Zhao, J.; Xia, J.; Wang, L.; Lai, W.-Y.; Pang, H.; Huang, W. Room temperature synthesis of cobalt-manganese-nickel oxalates micropolyhedrons for high-performance flexible electrochemical energy storage device. Sci. Rep. 2015, 5, 8536.

30. Pu, T.; Li, J.; Jiang, Y.; Huang, B.; Wang, W.; Zhao, C.; Xie, L.; Chen, L. Size and crystallinity control of two-dimensional porous cobalt oxalate thin sheets: tuning surface structure with enhanced performance for aqueous asymmetric supercapacitors. Dalton Trans. 2018, 47, 9241.
31. Zhao, C.; Jiang, Y.; Liang, S.; Gao, F.; Xie, L.; Chen, L. Two-dimensional porous nickel oxalate thin sheets constructed by ultrathin nanosheets as electrode materials for high-performance aqueous supercapacitors. CrystEngComm 2020, 22, 2953.
32. Liu, T.; Shao, G.; Ji, M.; Ma, Z. Composites of olive-like manganese oxalate on graphene sheets for supercapacitor electrodes. Ionics 2014, 20, 145−149.